Remote Sensing of Environment 200 (2017) 250–262

Contents lists available at ScienceDirect

Remote Sensing of Environment

journal homepage: www.elsevier.com/locate/rse

Combining hectometric and decametric satellite observations to provide near real time decametric FAPAR product

Wenjuan Li[a,*], Frédéric Baret[a], Marie Weiss[a], Samuel Buis[a], Roselyne Lacaze[b], Valerie Demarez[c], Jean-francois Dejoux[c], Marjorie Battude[c], Fernando Camacho[d]

[a] INRA-EMMAH, UMR 1114, 228 route de l'Aérodrome CS 40509, 84914 Avignon Cedex 9, France
[b] HYGEOS, Euratechnologies, 165 Avenue de Bretagne, 59000 Lille, France
[c] CESBIO, Université de Toulouse, CNES/CNRS/IRD/UPS, 18 avenue Edouard Belin, 31401 Toulouse Cedex 4, France
[d] EOLAB, Parc Cientific Universitat de Valencia, C/Catedrático Agustín Escardino, 9, 46980 Paterna, Valencia, Spain

ARTICLE INFO

Keywords:
FAPAR
Decametric
Hectometric
Near real time
Landsat-8
GEOV3
Data fusion

ABSTRACT

A wide range of ecological, agricultural, hydrological and meteorological applications at local to regional scales requires decametric biophysical data. However, before the launch of SENTINEL-2A, only few decametric products are produced and most of them remain limited by the small number of available observations, mostly due to a moderate revisit frequency combined with cloud occurrence. Conversely, kilometric and hectometric biophysical products are now widely available with almost complete and continuous coverage, but the associated spatial resolution limits the application over heterogeneous landscapes. The objective of this study is to combine unfrequent decametric spatial resolution products with frequent hectometric spatial resolution products to improve the temporal frequency and completeness of decametric observations. The study focuses on the fraction of photosynthetically active radiation absorbed by the green vegetation (FAPAR) because of its important role in canopy models and small dependency to scaling issues.

An algorithm is developed to provide near real time estimates of FAPAR called DHF (for Decametric Hectometric Fusion) at a decametric resolution and dekadal time step. It is assumed that the FAPAR time course is described by a second-degree polynomial function over a limited 60-days temporal window for each decametric pixel. To reduce the dimensionality of the problem, landcover classes are considered instead of each individual pixel. For each class, the coefficients of the polynomial function are adjusted using the temporal course of the available decametric FAPAR products, under the constraint of providing a good match with the time course of the hectometric dekadal FAPAR products. The point spread function associated to the hectometric FAPAR products and the possible biases between the decametric and hectometric FAPAR products are explicitly accounted for.

The algorithm was evaluated over a time series of decametric Landsat-8 FAPAR images (30 m) and hectometric (330 m) dekadal GEOV3 FAPAR derived from PROBA-V images acquired in 2014 over a site in the South-West of France.

Results show that the estimated DHF FAPAR products capture well the expected seasonal variation and spatial distribution while improving the temporal frequency and spatial and temporal completeness of the original Landsat-8 products. A leave one out exercise shows that the DHF values are in very good agreement with the Landsat-8 FAPAR (RMSE = 0.05–0.14) that were not used when computing the DHF. This demonstrates the robustness of the algorithm and interest under cloudy regions. Additional comparison with ground measurements collected over 14 sunflower fields along the growth season confirms the good performances of the DHF FAPAR products (RMSE = 0.11).

1. Introduction

A wide range of environmental and agricultural applications at local to regional scales requires accurate and frequent estimation of biophysical vegetation characteristics at the decametric spatial resolution. Satellite sensors such as Landsat-5 (30 m), Landsat-7 (30 m), Landsat-8 (30 m), SPOT4 (20 m), SPOT5 (20 m), FORMOSAT (8 m) and Sentinel-2A (10 m) provide observations at decametric resolutions.

* Corresponding author.
E-mail addresses: wenjuan.li@inra.fr, wenjuan.li122@gmail.com (W. Li).

http://dx.doi.org/10.1016/j.rse.2017.08.018
Received 31 October 2016; Received in revised form 31 July 2017; Accepted 14 August 2017

Several algorithms have already been proposed to generate biophysical products from these sensors, including Jiang et al. (2016), Li and Fang (2015), Li et al. (2015), Verger et al. (2011a), Verger et al. (2011c) and Ganguly et al. (2012). However, the use of these products is always limited by the reduced revisit frequency even degraded by cloud occurrence. Conversely, due to their large swath, kilometric resolution sensors such as VEGETATION, PROBA-V or MODIS provide daily observation of the globe. Few kilometric biophysical products have been generated operationally from these sensors at four to ten days interval, including MODIS (Knyazikhin et al., 1998), CYCLOPES (Baret et al., 2007), GEOV1 (Baret et al., 2013a), GEOV2 and GLASS (Liang et al., 2013; Xiao et al., 2015). They have been extensively validated and applied in several studies (Camacho et al., 2013; Garrigues et al., 2008; Weiss et al., 2007). However, the generally mixed nature of kilometric pixels raises both a scaling issue and difficulties when the landscape object of interest is significantly smaller than the pixel size (Baret et al., 2013a; Shabanov et al., 2003). Recent improvement of the spatial resolution down to hectometers such as PROBA-V (daily 330 m), Sentinel-3 (every 2 days, 300 m), and VIIRS (daily 370 m) is expected to get closer to the spatial resolution required for several applications. However, this is still far from the expected decametric resolution, more suited to the typical length scale of most landscapes (Garrigues et al., 2008).

The current technological constraints of sensors having only a limited number of pixels prevent from getting at the same time a large swath enabling frequent global coverage and keeping a sufficiently high spatial resolution. Constellation of high spatial resolution satellites may solve the question at the expense of an increased cost. Alternatively, the combination of decametric satellite observations with frequent hectometric or kilometric observations is a promising way to increase the temporal frequency of decametric products. Previous studies have demonstrated the ability of fusing observations at different spatial resolutions (Cardot et al., 2008; Faivre and Fischer, 1997; Gao et al., 2006; Hilker et al., 2009; Jiang et al., 2016; Zhu et al., 2015). These methods can be divided into several groups depending on (1) if the land cover map is used; (2) if time series information is used; and (3) if biophysical variables are estimated.

Faivre and Fischer (1997) used a linear unbiased prediction method to estimate reflectance at 20 m spatial resolution from an image with resolution of 400 m by assuming that the reflectance of a mixed pixel is a linear combination of several high resolution pure pixels. This method was later extended to LAI estimation (Faivre and Delecolle, 1997). Under the same assumption, Cardot et al. (2008) proposed a non-parametric statistical model to derive high spatial resolution reflectance or vegetation index from the temporal trajectory of frequent low spatial resolution data. This method was applied by Guyon et al. (2011) to monitor the phenology specific to the deciduous forest from kilometric satellite data. Both methods assume the a priori knowledge of the land cover at the decametric resolution. This constitutes a strong limitation of these methods, particularly over agricultural landscapes where the land cover may change significantly within a single year.

Gao et al. (2006), Hilker et al. (2009) and Zhu et al. (2010) proposed a method to fill gaps in Landsat surface reflectance images using MODIS data over a limited spatial window centered on the missing Landsat pixels. These algorithms do not require ancillary land cover map. However, they need a MODIS image close to the prediction time and are highly dependent on the number of input images (Gevaert and García-Haro, 2015). These requirements may limit the application of these methods in cloudy regions. Alternative methods performing only over multi-year time series of Landsat surface reflectance images have contributed to improve the spatial and temporal completeness of data (Zhu et al., 2015). However, the high dependency of these methods to the availability of Landsat clear images may be limiting in regions with high cloud occurence.

Data fusion methods were proposed for some variables including land surface temperature (Weng et al., 2014) and evapotanspiration (Anderson et al., 2011; Semmens et al., 2016). However, only little attention was paid to biophysical variables such as FAPAR or LAI (Jiang et al., 2016). The fusion of individual biophysical products derived from several sensors accounts implicitly for the differences between their observational characteristics since they are already explicitly used when computing the individual biophysical products. Current kilo/hectometric biophysical products show a good continuity and completeness in both the spatial and the temporal domains. The quasi dekadal temporal sampling also satisfies the requirements of several applications. Jiang et al. (2016) generated spatial consistent and complete Landsat LAI products by fusing Landsat and MODIS reflectance observation using an ensemble of multiscale filter and canopy radiative transfer model inversion. However, this study receives only limited validation and has not been applied for multi-date estimations.

The objective of this study is to develop an algorithm generating near real time decametric FAPAR products at a dekadal time step called DHF (Decametric-Hectometric Fused) from the combination of available decametric and kilometric FAPAR products. The algorithm is applied to Landsat-8 FAPAR products (Baret et al., 2016) and GEOV-3 FAPAR products (Baret et al., 2013b) biophysical products to generate the dekadal 30 m FAPAR time series of DHF products. The study area, satellite data and ground measurements used for the validation are first presented. Then the principles of the algorithm are described. Finally, the performances of the algorithm and corresponding products are evaluated and the limits discussed.

2. Materials

2.1. Study area and ground measurements

The 30 km × 30 km study area is located in the Southwest of France (Fig. 1) (43.52° N, 1.18° E). Several crops including wheat, sunflower, barley, rapeseed and maize are covering most of the area. The site is conveniently located where two Landsat-8 neighboring tracks overlap, offering potentially one image every 7 to 9 days at minimum.

FAPAR was measured six times in the sunflower fields of this region from June 12, 2014 to August 27, 2014, almost every 15 days, by using digital hemispherical photographs (DHP). In each field, a 20 m × 20 m Elementary sampling unit (ESU) was selected for the measurements (Fig. 1). Each ESU was sampled with 12–20 DHPs according to the VALERI spatial sampling protocol (http://w3.avignon.inra.fr/valeri). The DHPs were taken using a Nikon CoolPix 8400 camera equipped with a FC-E8 fisheye lens. The downward-looking camera was fixed at the top of a pole. The height of the pole keeps a constant distance (~1.2 m) between the lens and the top of the canopy (Demarez et al., 2008). All photos within an ESU were processed simultaneously using the CAN-EYE software (http://www4.paca.inra.fr/can-eye) to extract the FAPAR variable. The black-sky FAPAR (GCOS, 2011) observed at 10:00 solar time was used for the ground validation in this study was calculated from CAN-EYE.

2.2. LANDSAT-8 30 m FAPAR product

The derivation of FAPAR products from the Landsat-8 individual images at 30 m spatial resolution is achieved according to the algorithm described in Li et al. (2015). The Landsat-8 30 m FAPAR top of the atmosphere (TOA) reflectance images are first transformed into top of canopy (TOC) reflectance using the algorithm developed by Hagolle et al. (2008) and Hagolle et al. (2010). TOC reflectance in the green, red, near infrared and the two short wave infrared bands are then transformed into FAPAR values using a neural network, based on the BV-NNET (Biophysical Variables Neural Network) tool developed by Baret et al., 2007. FAPAR corresponds here to the black-sky value at 10:00 local solar time which provides a close approximation of the daily integrated black-sky value (Baret et al., 2007). The neural network was trained over a synthetic database made of PROSAIL radiative transfer

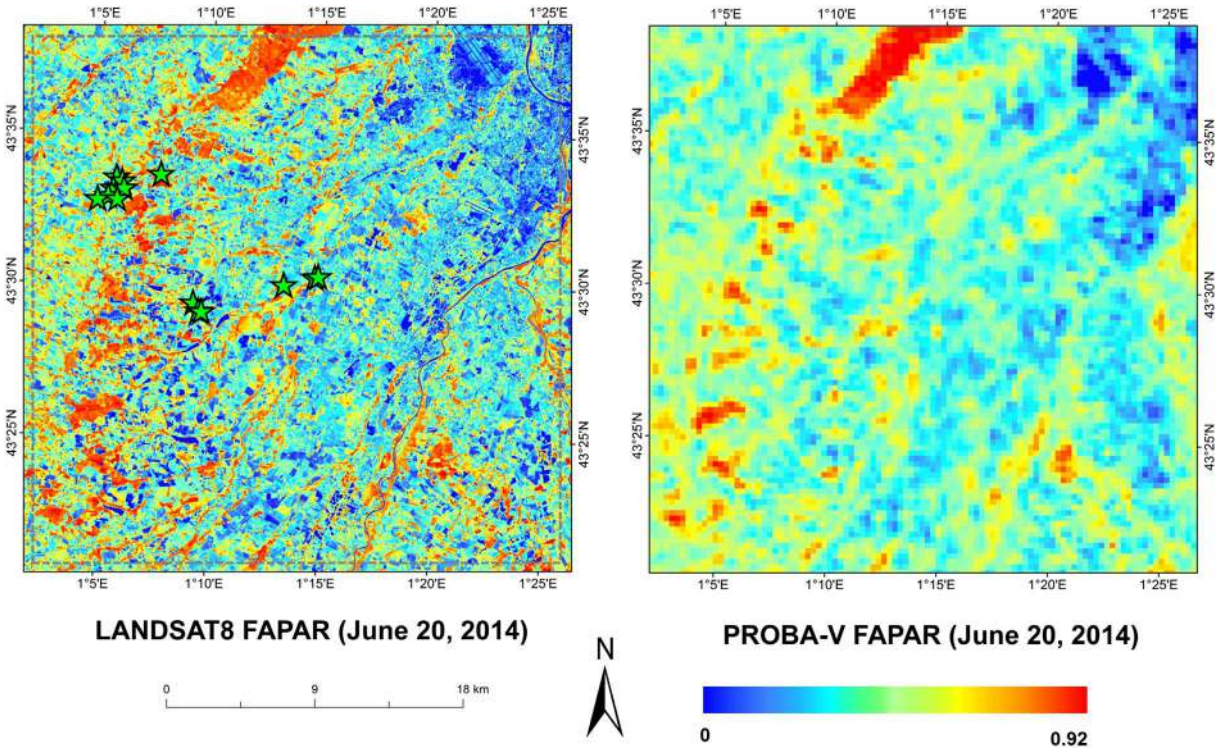

Fig. 1. (a) Landsat-8 FAPAR product and (b) PROBA-V FAPAR derived over the study area for June 20th 2014. Green stars represent the positions of ground measurements over sunflower fields in 2014. (For interpretation of the references to color in this figure legend, the reader is referred to the web version of this article.)

model simulations of TOC reflectance data (Jacquemoud et al., 2009). The distribution and co-distribution laws of the input variables of canopy structure, leaf and soil properties are designed to represent the expected actual distribution and co-distribution over the land surface. In addition to the FAPAR value, a quality flag is associated to each pixel to indicate the cloud contamination or cloud shadow, water or possible failure in the algorithm. The FAPAR 30 m product is provided in its original UTM projection on the WGS-84 datum and was validated over the same site of interest (R^2 = 0.86, RMSE = 0.1) (Li et al., 2015). The nominal Landsat revisit time is 16 days. However, the actual temporal sampling frequency of the FAPAR product derived from LANDSAT-8 varies from 7 to 16 days over the study area where 2 consecutive tracks overlap (Fig. S1).

2.3. GEOV3 FAPAR 330 m product

The FAPAR values at 330 m resolution are derived from the PROBA-V reflectance measurements according to the GEOV3 algorithm developed by Baret et al. (2013b). GEOV3 FAPAR is defined the same way as for Landsat-8. It is generated in near real time every ten days in two consecutive steps. In the first step, the daily FAPAR values are computed for each available PROBA-V observation using a neural network approach. The Neural network is trained over a specific data set corresponding to a weighted average of MODIS Collection5 and CYCLOPES V3.1 FAPAR products similarly to what was proposed by Baret et al. (2013a) for the GEOV1 products. The second step consists in compositing the daily FAPAR products to get the near real time final product at a dekadal time step by smoothing the temporal profile, filling possible gaps and making a short-term projection. Quality flags and quantitative uncertainties are also computed. The performances of GEOV3 products have been evaluated (R^2 = 0.84, RMSE = 0.1) (Camacho et al., 2016). GEOV3 products are provided in a plate carrée projection at 0.0089° spatial resolution (330 m at the equator) on WGS-84 datum. More details on the algorithm can be found in Baret et al. (2013b). The original GEOV3 products were projected in the UTM projection consistently with the Landsat-8 derived FAPAR products.

3. Methods

The general principles are first described with reference to decametric and hectometric FAPAR products. The implementation is then presented with application to LANDSAT-8 30 m and GEOV3/PROBA-V FAPAR products.

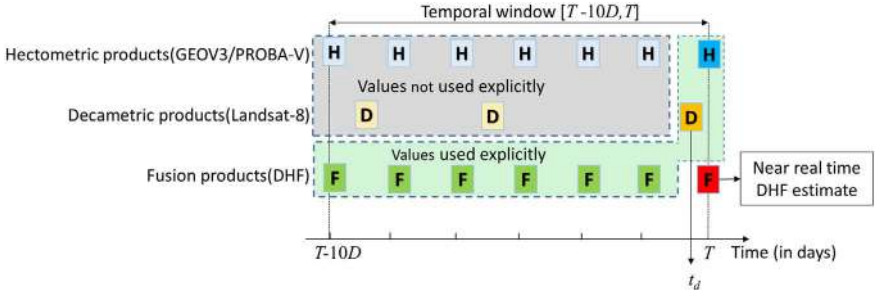

Fig. 2. The three available sources of FAPAR values used to compute the DHF FAPAR near real time estimates for the last dekad of the temporal window. t_d is the measurement date of Landsat-8, T is the last day of the temporal window and D is the length of temporal window expressed in dekads (here D = 6 dekads).

3.1. General principles

3.1.1. The fusion algorithm

The proposed algorithm is based on the combination of three FAPAR products (Fig. 2): (1) the hectometric GEOV3 FAPAR products available at the dekadal time step and derived from PROBA-V, $FAPAR^h$ (h stands for hectometric); (2) the decametric FAPAR products derived from Landsat-8, $FAPAR^d$ (d stands for decametric), available at a frequency ranging between 7 and 16 days with significant missing values due mainly to cloud occurrence; Fig. S1 in the supplementary information section describes the actual Landsat-8 available images and the corresponding percentage of valid pixels; (3) the previous DHF FAPAR products, $FAPAR^f$ (f stands for fusion), available at the decametric resolution and at the dekadal time step.

The computation of the DHF product for date T corresponding to the last day of the temporal window, composed of D dekads, rely on the previous time series of DHF products updated with the last hectometric product at time T (GEOV3/PROBA-V) and the possible decametric (Landsat-8) image available during the last dekad $[T-10, T]$. The other hectometric and possible decametric products existing within $[T-10D, T-10]$ temporal window are not explicitly taken into account in the algorithm since they have already been used to estimate the previous DHF products at T-10.

The algorithm assumes that the dynamics of $FAPAR$ of a given decametric pixel is described by a second degree polynomial in a restricted temporal window $[T-10D, T]$ where D is the length of the temporal window expressed in dekads:

$$FAPAR_i^d(t) = a_i + tb_i. + t^2 c_i \quad (1)$$

where $FAPAR_i^d(t)$ is the $FAPAR$ value at the decametric resolution d for pixel i and for time t and $[a_i, b_i, c_i]$ are the corresponding polynomial coefficients. This assumption is justified by the expected smooth temporal variation of $FAPAR$. Indeed, FAPAR is mainly driven by the green area index and therefore results from incremental processes of growth and senescence. Once the coefficients $[a_i, b_i, c_i]$ are estimated, the DHF value for time t = T is computed. This corresponds to a short-term projection of the polynomials since the last date with a decametric information is generally observed for t < T (see Fig. 2). When the resulting DHF product value at time T is out of the expected physical range for the vegetation canopies ($0 \le FAPAR \le 0.94$) including a small tolerance (± 0.05), it is considered as a missing value. When the FAPAR value is in the tolerance domain ($-0.05 \le FAPAR \le 0.00$ - or $0.94 \le FAPAR \le 0.99$) the DHF value is set to the closest bound of the physical range (0.00 or 0.94).

The coefficients $[a_i, b_i, c_i]$ are estimated by fitting Eq. (1) to the previous DHF products and the possible decametric Landsat-8 image available during the last dekad. In addition, the constraints imposed by the hectometric observations are exploited: the $FAPAR$ value of a pixel I at the hectometric resolution and time t, $FAPAR_I^h(t)$, is the weighted average of decametric resolution pixels $FAPAR^d(t)$ values because of the scaling properties of $FAPAR$ (Weiss and Baret, 2010):

$$FAPAR_I^h(t) = \sum_{i=1}^{k} PSF_i . FAPAR_i^d(t) \quad (2)$$

The weights are described by the point spread function (PSF_i) considering that a limited number (k) of decametric resolution pixels contribute significantly to each hectometric pixel. The PSF of the PROBA-V hectometric $FAPAR$ products must therefore be known. It is computed using quasi-simultaneous Landsat-8 and PROBA-V $FAPAR$ products as shown later. Then, a correction is applied to avoid possible bias between hectometric and decametric products that are derived from the different sensors and algorithms.

A cost function J that uses three sources of information is minimized to estimate the 3 polynomial coefficients over each decametric pixel. The cost function J is the weighted sum of the corresponding three components.

$$J = J_f + J_d + J_h \quad (3)$$

where J_f, J_d and J_h are the components of the cost function associated respectively to the fusion (DHF), decametric (Landsat-8) and hectometric (GEOV3/PROBA-V) $FAPAR$ data. The first component of the cost functions (J_f in Eq. (3)) measures the discrepancy between the fusion products estimated previously, $FAPAR_i^f(t)$, and the new estimated value, $\widehat{FAPAR_i^f(t)}$ computed with Eq. (1) for all the kN decametric pixels in the spatial window and all the first $D-1$ dekads of the temporal window:

$$J_f = \frac{1}{kND} \sum_{i=1}^{kN} \sum_{t=1}^{D} (FAPAR_i^f(t) - \widehat{FAPAR_i^f(t)})2 \quad (4)$$

The second component (J_d in Eq. (3)) measures the discrepancy between the decametric $FAPAR$ product derived from a possible observation at date t_d during the last dekad, $FAPAR_i^d(t_d)$, and the estimated DHF product for the same date, $\widehat{FAPAR_i^f(t_d)}$. It is computed over all the $\alpha 2N$ decametric pixels of the spatial window considered, where α is the resolution ratio, i.e. the hectometric spatial resolution divided by the decametric spatial resolution. In our case, the resolution ratio is close to 11.

$$J_d = \frac{1}{\alpha 2N} \sum_{i=1}^{\alpha 2N} (FAPAR_i^d(t_d) - \widehat{FAPAR_i^f(t_d)})2 \quad (5)$$

The third component of the cost function (J_h in Eq. (3)) measures the discrepancy between the hectometric products and the FAPAR values computed using the estimated decametric fusion products $\widehat{FAPAR_I^f(T)}$. This is evaluated over all the N hectometric pixels of the spatial window for the last date T of the temporal window. PSF_i corresponds to the PSF value for each pixel i that is computed in an independent step. This third component introduces constraints between the individual decametric pixels. Further, because of the PSF, J_h introduces also explicit dependency between neighboring hectometric pixels since common decametric pixels are shared by adjacent hectometric pixels.

$$J_h = \frac{1}{N} \sum_{I=1}^{N} (FAPAR_I^h(T) - \sum_{i=1}^{k} PSF_i \widehat{FAPAR_i^f(T)})2 \quad (6)$$

Note that the three terms of the cost function are normalized by the number of times the individual contributions are summed up, i.e. $[\frac{1}{kND}, \frac{1}{\alpha 2N}, \frac{1}{N}]$ respectively for $[J_f, J_d, J_h]$. If there is no decametric Landsat-8 images available for some temporal windows, J_d is set to zero. Moreover, J_h is set to zero when the hectometric pixel is invalid. Similarly, when the algorithm is initialized, no DHF products are available and J_f is set to zero.

3.1.2. Spatial and temporal operating windows

The spatial and temporal windows used in the algorithm must be specified. The temporal window should be long enough to provide sufficient DHF, decametric and hectometric data, while being short enough to describe the temporal profile faithfully by a second-degree polynomial function. Previous studies (Verger et al., 2011b) showed that a second degree polynomial describes accurately the temporal profile over a 60-days period in most of the cases. A 60-days temporal window provides 7 dekadal DHF values among which the last one is to be estimated, 0 to 5 potential decametric images in the case of the Landsat-8 sensor, and 7 dekadal hectometric FAPAR products (GEOV3/PROBA-V). A 60-days temporal operating window ($D = 6$) is therefore selected. The temporal window is moved towards the future with a dekadal time step. When initializing the algorithm, the temporal window may also be moved towards the past. In this case, the first DHF value among the 7 available one in the 60-days period will be estimated similarly as we will see later.

The size of the spatial operating window should allow accounting for the overlap of the PSF between hectometric pixels while being small enough to ease the computation. A 3 × 3 hectometric pixels window that corresponds to a square kilometer was selected. However, because the extent of the PSF is generally larger than the ground sampling distance (the length of a side of a pixel), a border with decametric pixels will also need to be accounted for. The center of the spatial moving window is moved sequentially over the center over all hectometric pixels in the image. Therefore, except for the borders, the coefficients of all the decametric pixels in Eq. (1) belonging strictly (PSF not accounted for) to a hectometric pixel is estimated 9 times. A weighted average of the 9 DHF FAPAR estimates is computed to provide a unique value:

$$FAPAR_i^f(T) = \sum_{r=1}^{9} \widehat{\omega(r)\, FAPAR_{i,r}^f(T)} \tag{7}$$

where $\widehat{FAPAR_{i,r}^f(T)}$ is the DHF estimates for pixel i at date T coming from one of the 9 spatial windows r and $\omega(r)$ is the associated weight. The weight, $\omega(r=1)$, of the window centered on the considered hectometric pixel is assigned to be equal to that of the other 8 surrounding pixels $\omega(r>1)$. Weights are thus computed as:

$$\omega(r=1) = 0.5;\ \omega(r>1) = 0.0625 \tag{8}$$

This averaging process stabilizes the solution and prevents from discontinuities between spatial windows.

3.1.3. Initialization of the algorithm

The algorithm requires 6 existing DHF dekadal values at each dekadal time step when running forward in near real time. When the algorithm is applied over the first temporal window of the time series, no DHF decametric products is available yet. An initialization process should therefore be developed to get a first estimate of the DHF. This is completed in two steps: (1) find along the available time series a temporal window that contains enough Landsat decametric images to provide a good estimate of the DHF products; (2) then run backward the algorithm from this initialization window to generate the DHF values down to the start of the first temporal window of the time series (Fig. 3). The algorithm is run in the forward regular mode as described in Fig. 2 to increase the time series by including the most recent dekads.

The initialization step should start by identifying the temporal operating window in the time series that provides the maximum number of Landsat-8 images with a maximum of valid pixels. The inputs of the processing for this first window include all the 7 dekadal hectometric FAPAR images and all the available decametric images. Outputs are the DHF products for the 7 dekadal dates. At least three Landsat-8 decametric images should be used. When it is not possible to find three Landsat-8 decametric images within a 60-day temporal window, the time period should be extended to include three decametric images. If the decametric images have invalid pixels, it is not possible to fill them with the DHF estimates since they do not exist yet. In this case, small clusters of invalid pixels are filled with the neighboring values. If larger clusters of invalid pixels are observed, specific actions are undertaken that will not be detailed here for the sake of brevity. The reader can find the full description in the product ATBD (Baret et al., 2016).

If the initialization temporal window does not correspond to the first temporal window of the time series, the backward mode is triggered. It runs similarly to what is described for the regular forward near real time mode, except that the DHF of the first dekad of the temporal window is estimated instead of the last one (compare Fig. 2 with Fig. 3). This process is repeated down to the start of the temporal series.

3.2. Calibrating the point-spread-function of hectometric FAPAR products

The weights, PSF_i, of the point spread function (Eq. (2)) describing the aggregation process of decametric images to obtain the equivalent hectometric values need thus to be estimated. They account for several factors (Weiss et al., 2007) including the PSF of the instrument for each band, the geolocation uncertainty, the effect of the reprojection (from raw images to plate-carrée then to UMT), the atmospheric scattering, the viewing geometry and the temporal compositing of the daily hectometric images to produce the dekadal FAPAR values (Baret et al., 2013b). The PSF is described by truncated Gaussian functions using the Full Width at Half Maximum independently for the longitudinal ($FWHM_x$) and the latitudinal ($FWHM_y$) directions (Mira et al., 2015). The PSF is truncated when > 95% of the contribution to the signal is reached. The total extent of the PSF defined by ($Xmax, Ymax$) thus depends on the FWHM. Because of possible geolocation differences between the hectometric and decametric images, a shift in East-West (Δx) and North-South (Δy) directions is also considered. The four unknowns $[FWHM_x, FWHM_y, \Delta x, \Delta y]$ are retrieved by maximizing the correlation coefficient between the aggregated decametric (Landsat-8) FAPAR images and the hectometric (GEOV3) FAPAR products according to the scheme shown by Mira et al. (2015). For each image pair of decametric and hectometric images with about the same date, the $[FWHM_x, FWHM_y]$ are allowed to vary from 120 m to 960 m by 30 m steps in both directions, while the Landsat-8 shifts, $[\Delta x, \Delta y]$ varied from − 330 m to 330 m by 15 m steps. In total, 379,456 combinations of PSF values in x and y directions are generated and the one providing the highest correlation between the actual GEOV3 FAPAR and the aggregated Landsat-8 FAPAR is selected. The aggregated pixels that include invalid Landsat-8 pixels are discarded from the computation.

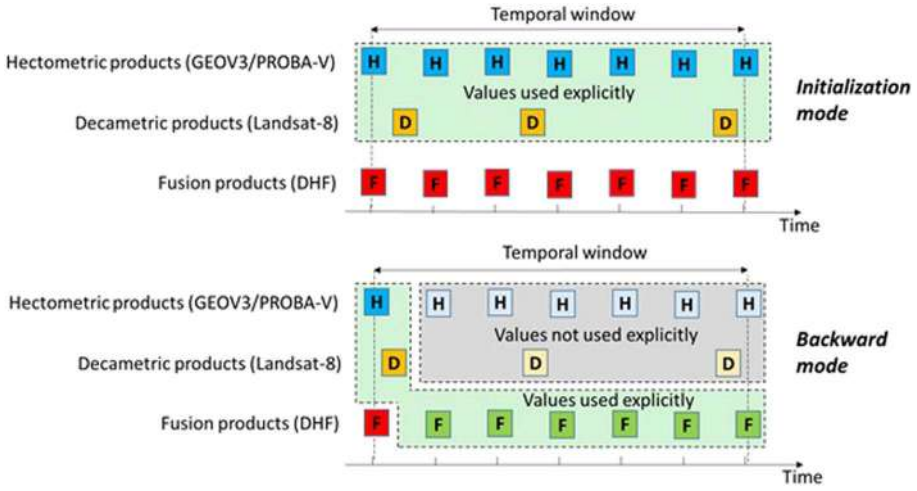

Fig. 3. Scheme showing the initialization and backward modes. The same conventions as used in Fig. 2 to describe the forward mode are used here.

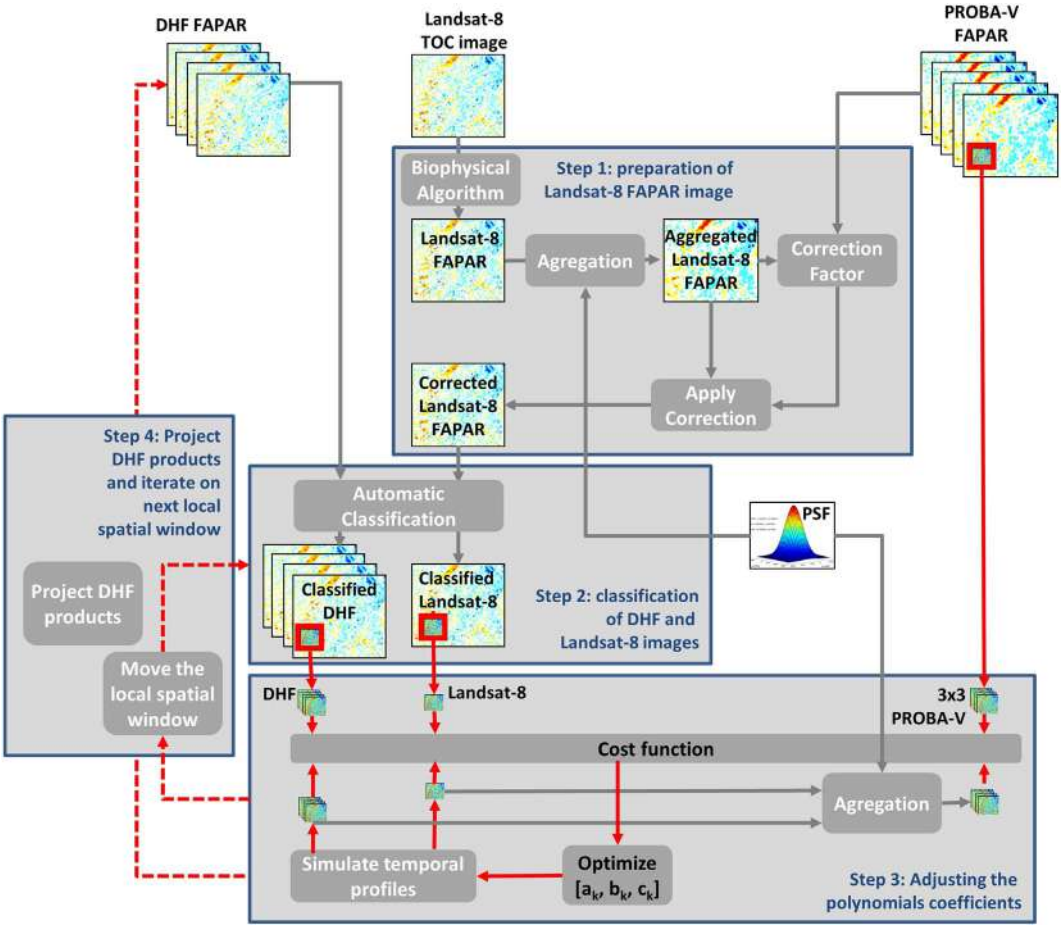

Fig. 4. Flowchart of the four steps of fusion main algorithm.

3.3. Implementation

The algorithm includes four steps: (1) preparation of the decametric images to fill possible invalid pixels and make the FAPAR values consistent with the hectometric products; (2) classification of the pixels to reduce the dimensionality of the problem; (3) adjusting the polynomial coefficients; (4) and production of the DHF FAPAR value and iterate on the next local spatial window. These four steps are sketched in Fig. 4 and detailed in the following.

3.3.1. Preparation of the decametric Landsat-8 FAPAR images (step1)

The algorithm combines hectometric resolution data (GEOV3/PROBA-V) with decametric resolution data (Landsat-8) when available. The aggregation process described by Eq. (2) requires completeness of the Landsat-8 image. When a Landsat-8 pixel is flagged as invalid, cloud or cloud shadow, it is filled using an estimation derived from a second degree polynomial fit over the 6 corresponding DHF values in the considered temporal window. When the estimated value is outside the [0, 0.94] domain of validity for FAPAR, it is set to the closest bound. This filling process is thus fully consistent with the way DHF products are generated.

The combination of Landsat-8 and GEOV3/PROBA-V resolution FAPAR data requires a high degree of consistency between both products. However, some biases may be observed due to differences between sensor characteristics, atmospheric correction or retrieval algorithms. A correction is therefore necessary to remove these differences to keep high degree of consistency between the two products. This correction is applied to the Landsat-8 images that may show less temporal consistency as compared to the GEOV3 FAPAR products that already results from a temporal compositing. It is calibrated on each individual Landsat-8 image by comparing the aggregated Landsat-8 FAPAR values using Eq. (2), with the GEOV3 FAPAR value estimated at the same date. For this purpose, a second-degree polynomial interpolation is applied using the 7 dekadal GEOV3 products available over the temporal operating window. Finally, a linear fit between the aggregated Landsat-8 FAPAR values and the corresponding interpolated GEOV3 FAPAR values is computed. The corresponding slope and intercept are used to correct the Landsat-8 FAPAR values.

3.3.2. Considering classes rather than pixels and classification (step2)

Running the algorithm over all individual decametric pixels is computationally very demanding. It was therefore preferred running it at the class level considering that a limited number of classes may represent the dynamics of each Landsat-8 pixel with a good accuracy in a restricted spatial and temporal window. A classification of each pixel is made using the FAPAR temporal profiles described by the 6 first DHF products and the possible Landsat-8 images available. The classification is applied over the whole image rather than over the local operating spatial windows to prevent from possible discontinuities between operating spatial windows. The 'Kmeans' automatic classification algorithm is used because of its performances and computational efficiency (Hartigan and Wong, 1979). The algorithm requires the number of classes to be specified. It should compromise between a large number required to accurately describe the heterogeneity of the study area and a limited number of classes to ease the computation. In our case, after trial and error tests (results not presented for the sake of brevity) 25 classes were selected as optimal. The reduction of the problem size is thus drastic: 25 sets of coefficients to be estimated in a 3×3 hectometric window as compared to > 900 sets of coefficients when considering the pixels separately.

3.3.3. Estimating $[a_k, b_k, c_k]$ coefficients for each class (step3)

The 3 coefficients of the second degree polynomials are estimated for each individual operating spatial and temporal window according to the general principles presented earlier. The fitting of the three coefficients for the 25 classes is completed by minimizing the cost function [3] under the constraints that the estimated FAPAR values keep within the physical bounds of FAPAR. The interior-point algorithm (Byrd et al., 2000; Byrd et al., 1999) is used to estimate coefficients $[a_k, b_k, c_k]$ simultaneously for the 25 classes. This algorithm is selected due to its ability to handle large and sparse optimization problems. The values from the previous dekad of the same temporal window are used as the initial guess for the three coefficients of each class. Finally, the FAPAR value for the last dekad (respectively every dekads for the initialization, and first dekad for the backward mode) of the temporal window is computed for each class and then distributed on the spatial operating window according to the classification map of the corresponding current temporal window.

3.3.4. Project DHF products and iterate on the next local spatial window (step4)

Once the polynomial coefficients of a spatial window are estimated, the DHF products corresponding to the decametric FAPAR values of the last day of the considered temporal window is computed. The algorithm then moves to the next local spatial window in an iterative way, until DHF FAPAR in all spatial windows are calculated. The new generated DHF FAPAR data will later participate to the computation of DHF for the next temporal window.

A quality flag associated to each dekad and pixel of the DHF product provides information on the number of valid Landsat-8 images available in the temporal window and the nature of the Landsat-8 pixel (out of range, cloud, water or snow). Further, two additional quantitative quality indicators document the difference (1) between the DHF product and the possible (corrected) Landsat-8 FAPAR value at the date of this Landsat-8 image, and (2) between the aggregated DHF value and the corresponding GEOV3 FAPAR product. Finally, when the estimated FAPAR value is out of range (including the tolerance margins), a specific flag is raised.

4. Results

The calibration of the GEOV3 PSF is first presented. Then, the spatial and temporal consistency of the DHF products is discussed at the decametric and then at the hectometric resolutions. Finally, the DHF products are compared with available ground measurements for accuracy assessment.

4.1. PSF of the GEOV3 products

We selected six pairs of GEOV3 and Landsat-8 FAPAR images having less than two days difference on which we adjusted the $[FWHM_x, FWHM_y, \Delta x, \Delta y]$ parameters (Table 1). Results show that the correlation between the aggregated Landsat-8 values and the GEOV3 products is always very high (Table 1), providing confidence in the parameter adjustment. Further, a single prominent maximum of the correlation coefficient was observed for all the dates when the PSF was evaluated, confirming the uniqueness of the solution. The optimal FWHM varies from 270 m to 360 m in the East-West direction, and from 330 m to 360 m in the North-South direction. This led to a PSF full extent of $810\,m \le X_{max} \le 870\,m$ and $690\,m \le Y_{max} \le 870\,m$, i.e. between two to three times the GEOV3 ground sampling distance (330 m). The shift between Landsat-8 and GEOV3 is around 100 m and is relatively constant with time. It is close to 0.3 PROBA-V pixels that correspond to the expected geolocation uncertainty.

Because of the good consistency in the PSF and shift values obtained across several pairs of Landsat-8 and GEOV3 images, it was proposed to calibrate the PSF only once over a set of pairs of Landsat-8 and GEOV3 images before triggering the fusion algorithm. The median value of the PSF and shift observed over the 6 pairs of images (Table 1) were used in this study for all the Landsat-8 and GEOV3 images over the South-West site in 2014: $[FWHM_x, FWHM_y, \Delta x, \Delta y] = [330, 360, 105, 75]$. However, the PSF probably needs to be recalibrated from site to site, particularly when the latitude changes because of the impact of the re-projection of the GEOV3 images into the Landsat-8 grid system.

Finally, the linear relationship between the aggregated Landsat-8 and GEOV3 FAPAR products provides a correction for the Landsat-8 FAPAR ($FAPAR_{Landsat\_8}{}^{original}$), to get values ($FAPAR_{Landsat\_8}{}^{corrected}$) that are more consistent with the GEOV3 FAPAR. Results over the six pairs of images show that the correction equation appears relatively stable for the study area (Table 1):

$$FAPAR^{corrected}_{Landsat,8} = 0.84 FAPAR^{original}_{Landsat,8} + 0.11 \quad (9)$$

4.2. Consistency between DHF and Landsat-8 FAPAR products

4.2.1. Temporal consistency

A sample of four pixels located on the edge and center of the image is used to illustrate the temporal consistency of the products. The original Landsat-8 FAPAR shows artifacts and gaps over the whole year (Fig. 5), confirming the observations by Li et al. (2015). This may be due to residual effects of the atmospheric correction and possible directional effects that are poorly accounted for. The correction of Landsat-8 FAPAR values achieved using the GEOV3 FAPAR as a reference (see §3.3.1) improves the smoothness. However, some fluctuations are still observed probably because the correction is computed over all the GEOV3 pixels, averaging possible particularities on some decametric pixels.

The DHF temporal profile is much smoother than that of the corrected Landsat-8 (Fig. 5). This comes mainly from the polynomials fitting and partly from a possible class averaging effect as well as smoothness induced by the GEOV3 constraint. However, the general agreement between DHF and Landsat-8 corrected FAPAR temporal

Table 1
The optimal PSF and shift observed over the 6 pairs of Landsat-8 and GEOV3 FAPAR products. $FWHM_x$ (respectively $FWHM_y$) represents the Full Width at Half Maximum in the East-west (respectively North-south) directions. X_{max} (respectively Y_{max}) represents the full width of the PSF in the East-west (respectively North-south directions).Δx (respectively Δy) represents the Landsat-8 image shift in East-west (respectively North-south) directions with the starting reference on the top-left corner of GEOV3 pixel.

Date		FWHM (m)		Full width (m)		Shift (m)		R^2	Correction		
GEOV3	Landsat-8	$FWHM_x$	$FWHM_y$	X_{max}	Y_{max}	Δx	Δy		Slope	Offset	RMSE
10/02/2014	12/02/2014	330	360	870	810	105	75	0.83	0.84	0.07	0.07
10/03/2014	09/03/2014	360	360	870	870	105	105	0.87	0.92	0.08	0.08
10/04/2014	10/04/2014	330	360	870	810	105	75	0.88	0.84	0.07	0.07
20/05/2014	19/05/2014	270	330	810	690	75	15	0.85	0.79	0.08	0.08
20/06/2014	20/06/2014	330	360	870	810	105	75	0.87	0.80	0.05	0.05
31/08/2014	01/09/2014	330	360	870	810	105	75	0.92	0.94	0.07	0.07
Median		330	360	870	810	105	75	0.87	0.84	0.11	0.07

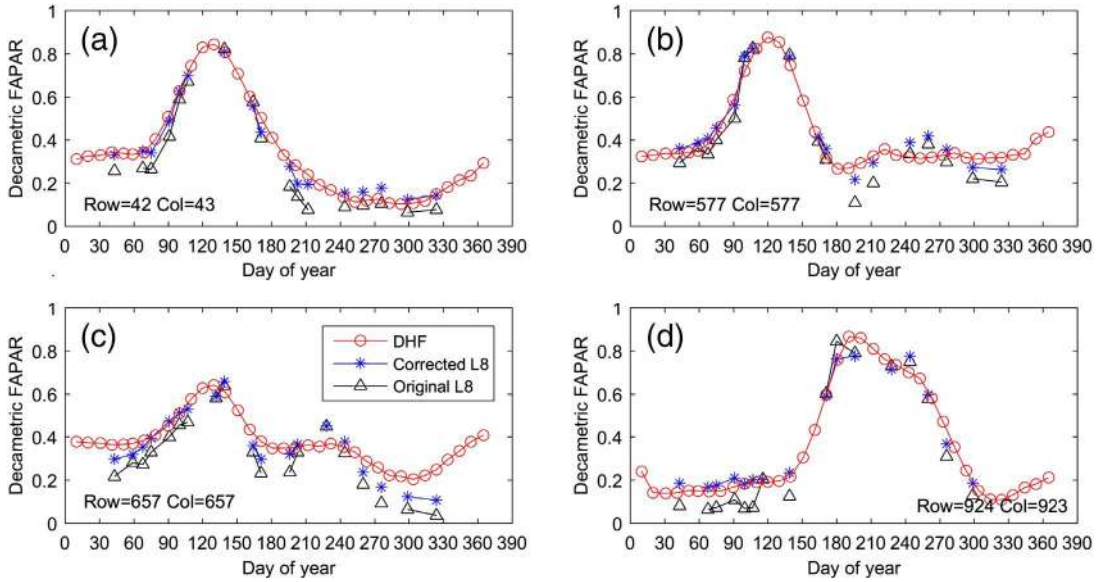

Fig. 5. Temporal distribution of DHF FAPAR, corrected Landsat-8 FAPAR and original Landsat-8 FAPAR over the four sample pixels in 2014. Row and Col correspond to the position of the decametric pixel in the whole 30 km × 30 km study area (Fig. 1).

profiles indicates that very little information was lost when operating the algorithm at the class level rather than at the pixel level. The predicting capacity of the algorithm is demonstrated at the beginning of the year when no Landsat-8 images are available: in this case, DHF provides reasonable estimates of FAPAR using the information coming from the GEOV3 FAPAR.

4.2.2. Spatial consistency

The spatial distribution of DHF FAPAR products is evaluated by mapping the difference with the original Landsat-8 FAPAR and corrected Landsat-8 FAPAR over two particular dates.

On March the 16th corresponding to the first temporal window (DOY 41–DOY 100), the original Landsat-8 FAPAR is almost complete (no clouds), although it shows several small gaps due to the input reflectance or output FAPAR out of the expected range as well as gaps on the border of the image (Fig. 6a). The corrected Landsat-8 FAPAR shows the same gaps as in the original Landsat-8 FAPAR image because no temporal interpolation is performed in the first temporal window. The estimated DHF image (Fig. 6c) presents a spatial distribution very close to the corrected Landsat-8 images (Fig. 6b) with a RMSE value of 0.04 (Fig. 6d). The larger differences between DHF and original Landsat-8 FAPAR are mainly due to the inherent bias between Landsat-8 and GEOV3 FAPAR. Note that the DHF image (Fig. 6c) presents a border of 330 m width with missing values due to the PSF effect of GEOV3 products.

On the 31st of July, the algorithm is run in the forward mode (DOY 161–DOY 222). The Landsat-8 original image shows a significant fraction of pixels contaminated by clouds (Fig. 7a). Cloudy pixels are filled with the values computed from the polynomial fit of the existing DHF values. The correction factor to get Landsat-8 FAPAR values consistent with those of GEOV3 may therefore be slightly biased. Indeed, the cloudy pixels are filled with DHF products generated from already corrected FAPAR values. The bias should therefore be maximum when clouds represent 50% cover fraction. However, the gap filling is mandatory since the computation of the correction requires aggregating the Landsat-8 pixels to be compared with those of GEOV3. But the projection corresponding to the application of the polynomial function on dates out of the period where it was adjusted can lead to values out of the expected range. These pixels will be flagged as invalid and will not be used (Fig. 7b). The DHF derived FAPAR (Fig. 7c) shows a complete spatial coverage and agrees well with the corrected Landsat-8 FAPAR (Fig. 7d), with however degraded performances (RMSE = 0.08) due to the presence of clouds and the associated loss of information. Nevertheless, the spatial patterns appear quite well preserved, even at the location of the clouds on the Landsat-8 image.

4.2.3. Validation of DHF using the leave-one-out method

The performances of the DHF products are evaluated by comparison with each individual Landsat-8 derived FAPAR values. However, to better evaluate the accuracy of the DHF products without comparing

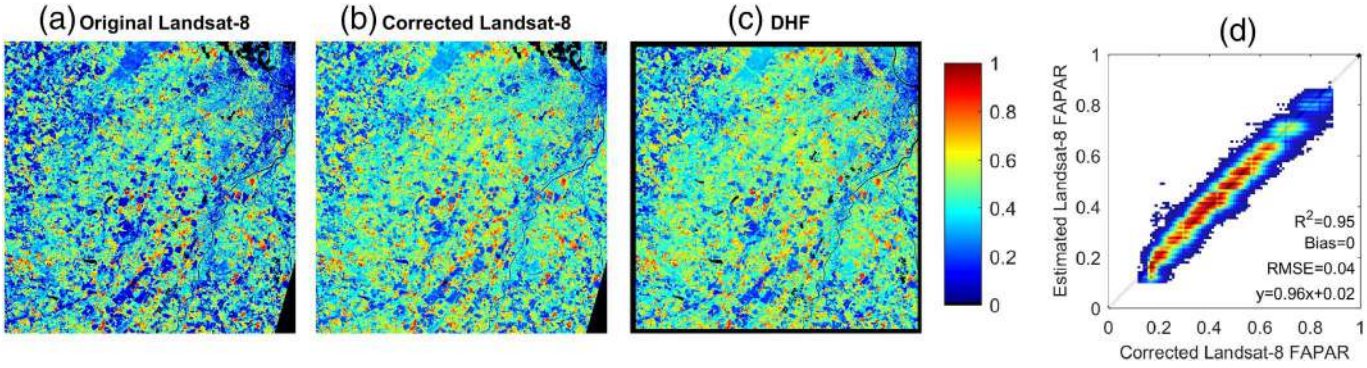

Fig. 6. Spatial distribution observed over Southwest site on 16 March 2014 of (a) the original Landsat-8 FAPAR; (b) the corrected Landsat-8 FAPAR; (c) the DHF FAPAR; (d) the relationship between the corrected Landsat-8 and the DHF FAPAR values. Black pixels represent invalid pixels due to clouds, cloud shadow, water, snow or image borders.

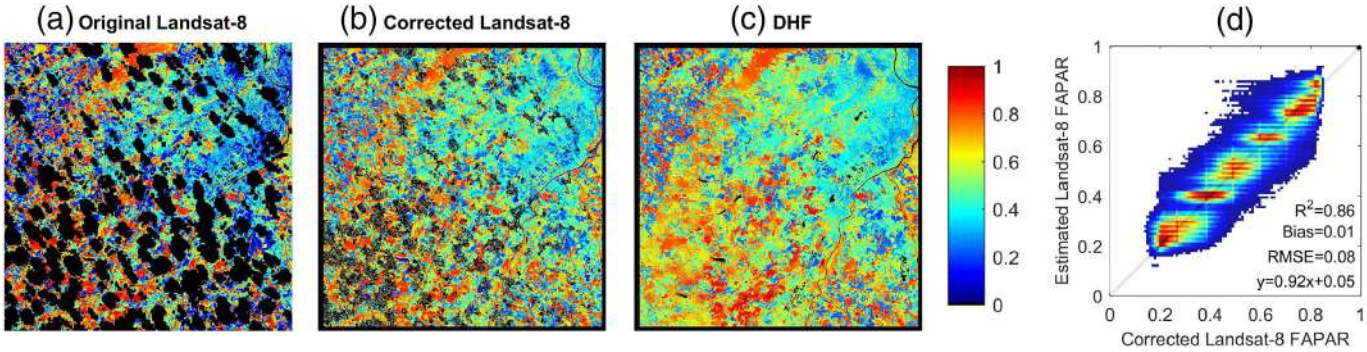

Fig. 7. Spatial distribution observed over Southwest site on 31 July 2014 of (a) the original Landsat-8 FAPAR; (b) the corrected Landsat-8 FAPAR; (c) the DHF FAPAR; (d) the relationship between the corrected Landsat-8 and the DHF FAPAR values. Black pixels represent invalid pixels due to clouds, cloud shadow, water, snow or image borders.

with the Landsat-8 images that were used in the algorithm, a leave-one-out method was introduced: a Landsat-8 image will not be used in the algorithm and the resulting DHF product will be compared to this Landsat-8 image derived FAPAR values. This process is repeated on each Landsat-8 image of the time series. The initial temporal window is not used in the leave-one-out test, therefore the first Landsat-8 measurement date starts from DOY107 of 2014. This analysis is performed on a sub region of 5 km × 5 km area for computation efficiency. The DHF products are interpolated at the date of the Landsat-8 image. The comparison is achieved both with the original Landsat-8 derived FAPAR values as well as with the corrected Landsat-8 FAPAR values ensuring better consistency with the GEOV3 FAPAR products.

As expected, results show that the correction of the Landsat-8 derived FAPAR products improves significantly the agreement with the DHF products (Table 2). The correction improves the RMSE by 0.05, R^2 by 0.04 and the bias is reduced by 0.01 both for the leave-one-out DHF version (remove) and the DHF computed using all the Landsat-8 images (used) (Table 2).

The DHF computed with all the Landsat-8 images available used (used in Table 2) agrees well with the Landsat-8 corrected FAPAR values with $0.05 < RMSE < 0.12$, $0.66 < R^2 < 0.97$ and $-003 < bias < 0.03$ (Table 2). When comparing with the corrected Landsat-8 FAPAR image not used to compute the DHF product (remove in Table 2), the RMSE and R^2 degrades only slightly. This demonstrates the robustness of the proposed algorithm for estimating DHF FAPAR values on most situations. However, the algorithm partly fails on DOY171 (RMSE = 0.12 and R^2 = 0.47 in Table 2), when no Landsat-8 FAPAR is used to document the high rate of change of FAPAR profile as observed here during the senescence period of winter crops.

4.3. Consistency between aggregated DHF FAPAR and original GEOV3 FAPAR products

Four GEOV3 pixels located on the edge and center of the GEOV3 image are selected for visual inspection of the temporal consistency between the DHF FAPAR aggregated at GEOV3 FAPAR spatial resolution using the PSF (Eq. (2)) and the original GEOV3 FAPAR. Results (Fig. 8) confirm the expected very good agreement between the dynamics of both FAPAR values. However, some small differences are observed due to remaining discrepancies between the Landsat-8 FAPAR corrected values and the GEOV3 products.

The consistency between both products is further analyzed by comparing their spatial distribution for three specific dates: doy 10 in the backward mode, doy 100 in the first initial temporal window and doy 283 in the forward mode. Results (Fig. 9) show a very good agreement (R^2 = 0.81–0.9, RMSE = 0.03–0.06) between the aggregated DHF FAPAR images and GEOV3 FAPAR for these three dates. However, some missing values are observed on the aggregated DHF image. This can be due to FAPAR values estimated out of the physical range, which prevents from applying the aggregation process. These situations mostly correspond to low values of FAPAR and when a limited constraint by the Landsat-8 information is imposed because of large cloud contamination of the Landsat-8 images.

A systematic evaluation of the RMSE values computed over each

Table 2
RMSE, R^2 and Bias between DHF products and the original ('Original') or corrected ('Corrected') Landsat-8 products on each Landsat-8 measurement date. The DHF FAPAR products were generated using either all the Landsat-8 images available ('Used') or when the Landsat-8 image used for performance evaluation was removed ('Remove') from the time series for DHF computation using the leave-one-out method.

	Day of year												
	107	132	139	164	171	180	196	203	212	228	244	260	276
RMSE													
Remove/Original	0.115	0.095	0.138	0.100	0.133	0.156	0.171	0.139	0.135	0.159	0.161	0.175	0.164
Remove/Corrected	0.078	0.053	0.113	0.088	0.120	0.099	0.140	0.072	0.101	0.090	0.126	0.125	0.119
Used/Original	0.090	0.090	0.090	0.080	0.080	0.100	0.120	0.140	0.110	0.130	0.160	0.130	0.160
Used/Corrected	0.050	0.050	0.070	0.070	0.070	0.060	0.090	0.070	0.070	0.060	0.120	0.090	0.100
R^2													
Remove/Original	0.915	0.894	0.810	0.717	0.473	0.555	0.656	0.825	0.826	0.657	0.577	0.590	0.641
Remove/Corrected	0.915	0.957	0.810	0.727	0.471	0.705	0.684	0.909	0.828	0.853	0.578	0.590	0.641
Used/Original	0.960	0.918	0.933	0.818	0.800	0.826	0.878	0.815	0.907	0.815	0.660	0.759	0.748
Used/Corrected	0.960	0.965	0.933	0.824	0.799	0.884	0.884	0.909	0.908	0.905	0.661	0.759	0.748
Bias													
Remove/Original	0.058	− 0.019	0.054	− 0.020	0.008	− 0.013	0.004	− 0.022	0.053	− 0.065	0.054	0.095	0.079
Remove/Corrected	0.034	− 0.012	0.039	− 0.038	− 0.025	− 0.004	− 0.031	− 0.039	0.012	− 0.046	− 0.001	0.032	0.012
Used/Original	0.043	− 0.014	0.038	− 0.012	0.017	− 0.006	0.013	− 0.011	0.043	− 0.054	0.074	0.056	0.093
Used/Corrected	0.019	− 0.010	0.023	− 0.031	− 0.015	− 0.016	− 0.021	− 0.031	0.004	− 0.034	0.019	− 0.007	0.026

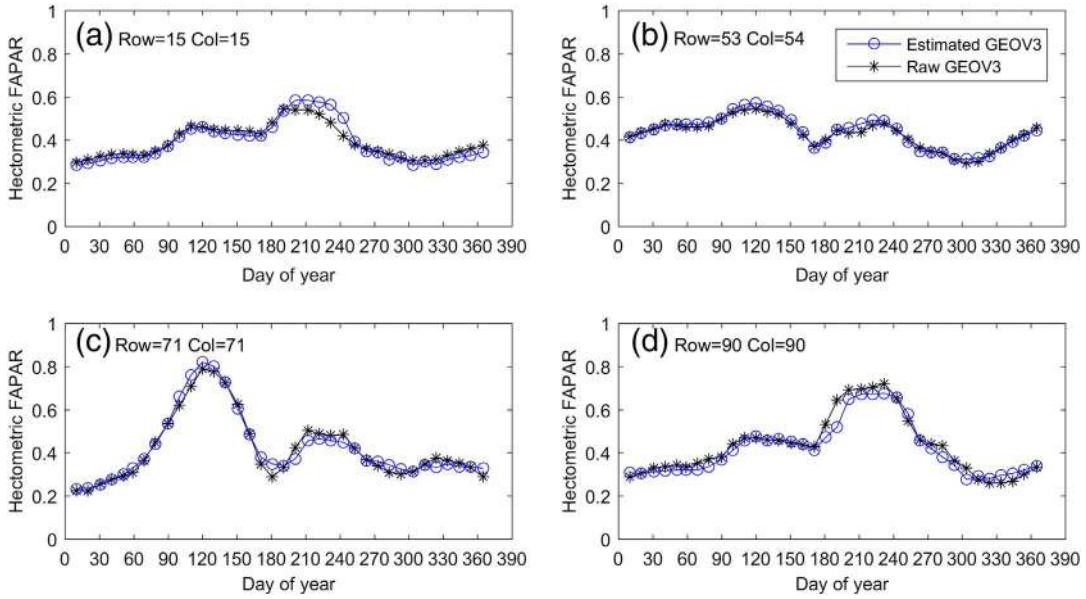

Fig. 8. Temporal distribution of estimated GEOV3 from aggregation of DHF FAPAR and original GEOV3 FAPAR profiles. Four sample pixels are selected on the center or edge of GEOV3 images.

dekad of the time series confirms the very good agreement between the aggregated DHF FAPAR products and the GEOV3 FAPAR values (Fig. 10). The RMSE ranges from 0.03 (DOY 31) to 0.08 (DOY 253).

4.4. Validation with ground measurements

The FAPAR values measured with DHP over the 14 sunflower ESUs available along the growing season are compared with the DHF and original or corrected Landsat-8 FAPAR values. To minimize the effect of the delay between the date of the ground measurements and that of the Landsat-8 FAPAR products, the ground FAPAR measurements are linearly interpolated at the Landsat-8 image acquisition dates if there is < 5 days difference. This resulted in 29 data points. Conversely, for comparing the DHF products with the ground measurements, the DHF products are interpolated at the ground measurements dates since DHF products are dekadal smooth products. Results focusing on the 29 data points used for comparison with the original or corrected Landsat-8 data show that the original Landsat-8 FAPAR correlates well with the ground measurements (Fig. 11a). The performances are only slightly improved after the correction using GEOV3 FAPAR (Fig. 11b). Both Landsat-8 FAPAR estimates have 75% of the points within the Global climate observing system (GCOS) requirements (dotted lines in Fig. 11) (max 10% accuracy, GCOS, 2011). Over the same 29 points, the performance of DHF FAPAR is very close to the original and the corrected Landsat-8 FAPAR data (Table 3). Finally, the DHF FAPAR products were compared with 36 additional available ground measurements over the sunflower fields. They correspond to ground data collected outside the ± 5 days period around the Landsat-8 image dates. Results over the total 65 point data available show a slight degradation of the performances (Fig. 11c, Table 3) with some underestimation for the medium to large FAPAR values. Nevertheless, still 75% of the points are lying within the GCOS requirements for FAPAR products.

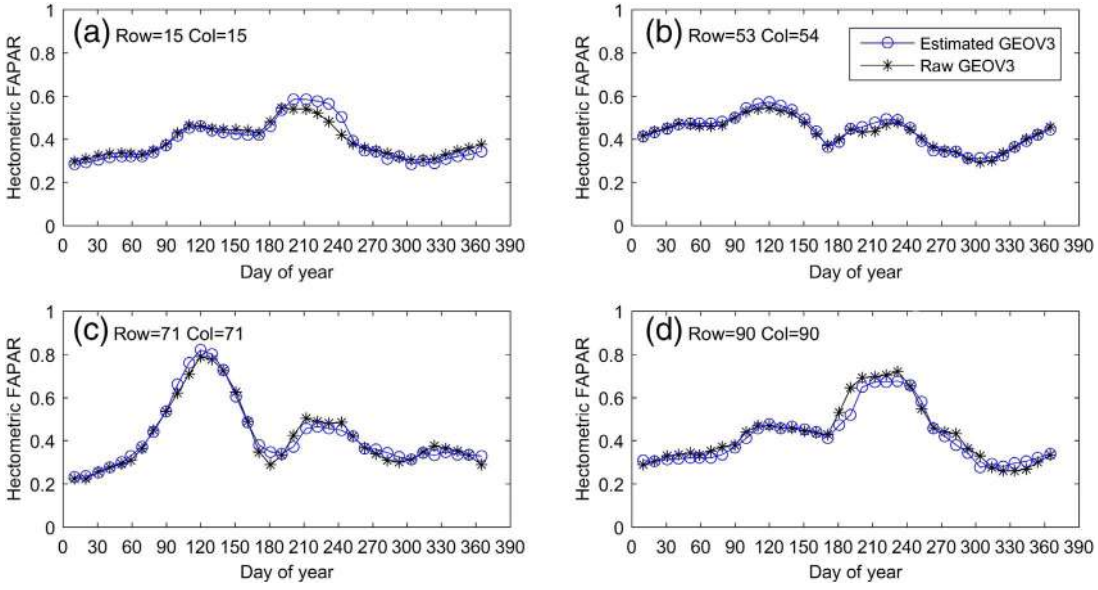

Fig. 9. Spatial distribution of (a, d, g) original GEOV3 FAPAR, (b, e, h) aggregated DHF FAPAR at GEOV3 spatial resolution and (c, f, i) frequency of their differences; (a, b, c) correspond to DOY 10, (d, e, f) to DOY 100 and (g, h, i) to DOY 283.

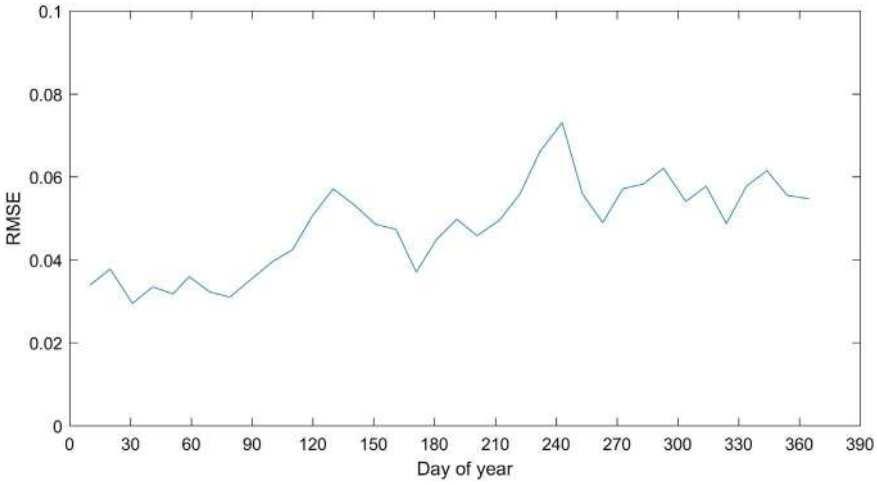

Fig. 10. The seasonal variation of RMSE between aggregated DHF FAPAR at GEOV3 spatial resolution and original GEOV3 FAPAR in 2014 over Southwest site.

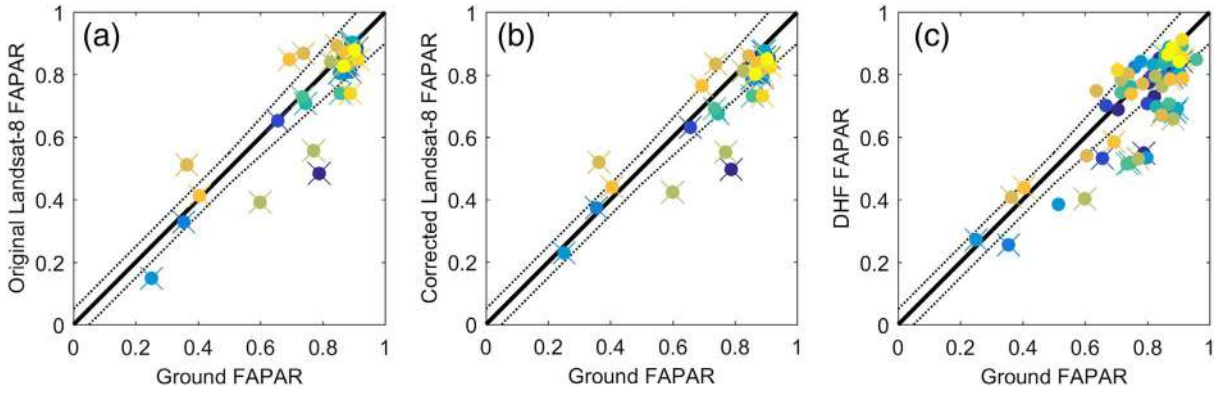

Fig. 11. Comparison of the ground FAPAR measurements with (a) the original Landsat-8 FAPAR, (b) the corrected Landsat-8 FAPAR and (c) the DHF FAPAR products. Results observed on 29 data points over the 14 sunflower fields. Each field corresponds to a particular color. The black solid line is the 1:1 line. Dotted lines represent the GCOS (2011) requirements boundaries.

Table 3
Comparison between the ground FAPAR measurements and the original Landsat-8 FAPAR, the corrected Landsat-8 FAPAR and the DHF FAPAR products. N represents the number of ground data used in the validation.

	N	R^2	Bias	RMSE	Linear regression
Original Landsat-8	29	0.76	− 0.04	0.104	y = 0.94x + 0.01
Corrected Landsat-8	29	0.78	− 0.05	0.102	y = 0.82x + 0.08
DHF FAPAR	29	0.75	− 0.09	0.12	y = 0.84x + 0.02
DHF FAPAR	65	0.66	− 0.07	0.11	y = 0.87x + 0.04

5. Discussion

The proposed DHF algorithm uses a biophysical product, FAPAR, which is assumed to present a smooth dynamics as outlined earlier. An alternative method was proposed by Lewis et al. (2012) using reflectance as inputs and outputs of an assimilation scheme. It preserves the spectral consistency thanks to a radiative transfer model. Such approaches are thus very appealing as already outlined by Geiger et al. (2004). The spectral consistency between the decametric and hectometric data is also well preserved in the DHF algorithm since the fusion between the two resolution data is achieved at the biophysical FAPAR product level.

The proposed DHF algorithm is based on a physically sound approach that bears on two main assumptions: (1) the smoothness of the FAPAR temporal course over a restricted temporal window (60 days in this case) and (2) the scaling independency of FAPAR. The first assumption is mostly verified over the study site considered here. However, it may be violated particularly in case of harvest occurring during the vegetation growth cycle such as for cultivated grasslands, silage maize, forest clear cut or when hazards are suddenly changing the surface characteristics such as fire or flood events. The second assumption on the scaling properties appears to be largely verified according to the good agreement observed between the decametric DHF or Landsat-8 aggregated FAPAR products and the GEOV3 hectometric products. The algorithm provides smooth and consistent FAPAR estimates at the decametric resolution, with an accuracy close to RMSE ≈ 0.1 while 75% of the values are within the GCOS requirements. The good performances of the algorithm are also coming from the fact that the hectometric constraint is relatively strong since only a limited number of classes of land cover are contained in a hectometric pixel as compared to what is contained in a kilometric pixel for which the constraint would be much weaker. Although the ground validation exercise was restricted to sunflower crops, the good agreement between the original Landsat-8 and the DHF values observed with the leave-one-out method indicates the potentials of the proposed method.

The performances of the DHF algorithm were evaluated using GEOV3/PROBA-V dekadal FAPAR products and Landsat-8 images over a place where the Landsat sensor swaths are overlapping between two consecutive tracks, dividing by about two the 16 days nominal Landsat-8 revisit period. Over the considered time series and site, the actual average delay between two consecutive clear pixels was around 20 days due to cloud coverage if the whole year is considered. It is reduced to around 12 days during the growing season because only few images are taken at the beginning or the end of year. The results of the leave-one-out validation test demonstrated that the performances are only little dependent on the presence of the last Landsat-8 image before the

considered dekadal date when the DHF product is computed. However, further investigation should evaluate the actual impact of the number of clear decametric observations on the product performances.

The recent availability of the Sentinel-2 (Drusch et al., 2012) and Sentinel-3 (Donlon et al., 2012) images will probably reinforce the interest of this type of algorithm, particularly in places with frequent cloud occurrence. The PSF of the FAPAR products derived at the hectometric resolution with Sentinel-3 should be properly calibrated. Although the PSF appeared to be relatively stable over time on the studied site, this should be further verified in more diversified situations, particularly regarding the expected effect of the latitude of the site.

6. Conclusion

This study presented an algorithm to generate a dekadal FAPAR product at decametric resolution from the combination of existing decametric (Landsat-8) and hectometric (GEOV3) FAPAR products. It applies to any vegetation type without prior knowledge on the land cover. The method can be run in near real time mode. The proposed method assumes that FAPAR time course can be described by a second-polynomial function during a 60-days temporal window for each decametric pixel. The coefficients of the polynomial function are optimized using temporal courses of the available Landsat-8 FAPAR and GEOV3 FAPAR. The generated DHF FAPAR captures faithfully the temporal and spatial distribution of Landsat-8 FAPAR, and improves the temporal resolution and smoothness of Landsat-8 FAPAR. Using the leave-one-out method, the DHF FAPAR products correspond well with the Landsat-8 FAPAR (RMSE = 0.05–0.14) that are not used in the DHF algorithm. The DHF FAPAR products show also good agreement with ground measurements over 14 sunflower fields (RMSE = 0.11, R^2 = 0.66). Further developments of the algorithm would include its application to the actual Sentinel-2 and Sentinel-3 datasets, as well as its adaptation to other biophysical variables such as LAI.

Supplementary data to this article can be found online at http://dx.doi.org/10.1016/j.rse.2017.08.018.

Acknowledgements

The authors are grateful for the financial support of FP7 IMPLEMENTING MULTI-SCALE AGRICULTURAL INDICATORS EXPLOITING SENTINELS (IMAGINES) project under Grant Agreement No. 311766. Hervé Gibrin, Arnaud Micheneau, Oliva Mas Erauso and Bernard Marciel are acknowledged for their help in ground measurements and Can-Eye processing. We would also gratefully thank the two anonymous reviewers for their thoughtful comments.

References

Anderson, M.C., Kustas, W.P., Norman, J.M., Hain, C.R., Mecikalski, J.R., Schultz, L., González-Dugo, M.P., Cammalleri, C., d'Urso, G., Pimstein, A., Gao, F., 2011. Mapping daily evapotranspiration at field to continental scales using geostationary and polar orbiting satellite imagery. Hydrol. Earth Syst. Sci. 15, 223–239.

Baret, F., Hagolle, O., Geiger, B., Bicheron, P., Miras, B., Huc, M., Berthelot, B., Niño, F., Weiss, M., Samain, O., Roujean, J.L., Leroy, M., 2007. LAI, fAPAR and fCover CYCLOPES global products derived from VEGETATION part 1: principles of the algorithm. Remote Sens. Environ. 110, 275–286.

Baret, F., Weiss, M., Lacaze, R., Camacho, F., Makhmara, H., Pacholcyzk, P., Smets, B., 2013a. GEOV1: LAI and FAPAR essential climate variables and FCOVER global time series capitalizing over existing products. Part1: principles of development and production. Remote Sens. Environ. 137, 299–309.

Baret, F., Weiss, M., Verger, A., Smets, B., 2013b. Algorithm Theoretical Basis Documents of LAI, FAPAR, FCover at 300m from PROBA-V(GEOV3). INRA, Avignon. http://fp7-imagines.eu/pages/documents.php.

Baret, F., Li, W., Weiss, M., Buis, S., 2016. ATBD OF 10-M (30-M) FAPAR FOR S2 (LANDSAT-8) AND S3 (+ PROBA-V). INRA, Avignon. http://fp7-imagines.eu/pages/documents.php.

Byrd, R.H., Hribar, M.E., Nocedal, J., 1999. An interior point algorithm for large-scale nonlinear programming. SIAM J. Optim. 9, 877–900.

Byrd, R.H., Gilbert, J.C., Nocedal, J., 2000. A trust region method based on interior point techniques for nonlinear programming. Math. Program. 89, 149–185.

Camacho, F., Cernicharo, J., Lacaze, R., Baret, F., Weiss, M., 2013. GEOV1: LAI, FAPAR essential climate variables and FCOVER global time series capitalizing over existing products. Part 2: validation and intercomparison with reference products. Remote Sens. Environ. 137, 310–329.

Camacho, F., Sánchez, J., Latorre, C., 2016. Gio Global Land Component – Lot I "Operation of the Global Land Component": Quality Assessment Report LAI, FAPAR, FCover Collection 300 m Version1. EOLAB, Valencia. http://land.copernicus.eu/global/sites/default/files/products/GIOGL1_QAR_FAPAR300m-V1_I1.10.pdf.

Cardot, H., Maisongrande, P., Faivre, R., 2008. Varying-time random effects models for longitudinal data: unmixing and temporal interpolation of remote-sensing data. J. Appl. Stat. 35, 827–846.

Demarez, V., Duthoit, S., Baret, F., Weiss, M., Dedieu, G., 2008. Estimation of leaf area and clumping indexes of crops with hemispherical photographs. Agric. For. Meteorol. 148, 644–655.

Donlon, C., Berruti, B., Buongiorno, A., Ferreira, M.-H., Féménias, P., Frerick, J., Goryl, P., Klein, U., Laur, H., Mavrocordatos, C., Nieke, J., Rebhan, H., Seitz, B., Stroede, J., Sciarra, R., 2012. The global monitoring for environment and security (GMES) sentinel-3 mission. Remote Sens. Environ. 120, 37–57.

Drusch, M., Bello, U.D., Carlier, S., Colin, O., Fernandez, V., Gascon, F., Hoersch, B., Isola, C., Laberinti, P., Martimort, P., Meygret, A., Spoto, F., Sy, O., Marchese, F., Bargellini, P., 2012. Sentinel-2: ESA's optical high-resolution mission for GMES operational services. Remote Sens. Environ. 120, 25–36.

Faivre, R., Delecolle, R., 1997. Synthetic map of crop leaf area index dynamics estimated with satellite data. In: MODSIM'97: International Congress on Modelling and Simulation. Hobart, Australie (p. 6).

Faivre, R., Fischer, A., 1997. Predicting crop reflectances using satellite data observing mixed pixels. J. Agric. Biol. Environ. Stat. 2, 87–107.

Ganguly, S., Nemani, R.R., Zhang, G., Hashimoto, H., Milesi, C., Michaelis, A., Wang, W., Votava, P., Samanta, A., Melton, F., Dungan, J.L., Vermote, E., Gao, F., Knyazikhin, Y., Myneni, R.B., 2012. Generating global leaf area index from Landsat: algorithm formulation and demonstration. Remote Sens. Environ. 122, 185–202.

Gao, F., Masek, J., Schwaller, M., Hall, F., 2006. On the blending of the Landsat and MODIS surface reflectance: predicting daily Landsat surface reflectance. IEEE Trans. Geosci. Remote Sens. 44, 2207–2219.

Garrigues, S., Lacaze, R., Baret, F., Morisette, J.T., Weiss, M., Nickeson, J.E., Fernandes, R., Plumme, S., Shabanov, N.V., Myneni, R.B., Knyazikhin, Y., Yang, W., 2008. Validation and intercomparison of global Leaf Area Index products derived from remote sensing data. J. Geophys. Res. 113.

GCOS, 2011. Systematic Observation Requirements for Satellite-Based Products for Climate, 2011 Update, Supplemental Details to the Satellite-Based Component of the Implementation Plan for the Global Observing System for Climate in Support of the UNFCCC (2010 Update). http://www.wmo.int/pages/prog/gcs/Publications/gcos-154.pdf.

Geiger, B., Samain, O., Baret, F., Hagolle, O., Bicheron, P., Roujean, J.-L., Franchistéguy, L., Leroy, M., 2004. Multi-sensor data fusion for deriving bio-physical variables in the Cyclopes project. In: I. International (Ed.), Geoscience and Remote Sensing Symposium, 2004. IGARSS '04. Proceedings. Anchorage, Alaska, USA.

Gevaert, C.M., García-Haro, F.J., 2015. A comparison of STARFM and an unmixing-based algorithm for Landsat and MODIS data fusion. Remote Sens. Environ. 156, 34–44.

Guyon, D., Guillot, M., Vitasse, Y., Cardot, H., Hagolle, O., Delzon, S., Wigneron, J.-P., 2011. Monitoring elevation variations in leaf phenology of deciduous broadleaf forests from SPOT/VEGETATION time-series. Remote Sens. Environ. 115, 615–627.

Hagolle, O., Dedieu, G., Mougenot, B., Debaecker, V., Duchemin, B., Meygret, A., 2008. Correction of aerosol effects on multi-temporal images acquired with constant viewing angles: application to Formosat-2 images. Remote Sens. Environ. 112, 1689–1701.

Hagolle, O., Huc, M., Pascual, D.V., Dedieu, G., 2010. A multi-temporal method for cloud detection, applied to FORMOSAT-2, VENμS, LANDSAT and SENTINEL-2 images. Remote Sens. Environ. 114, 1747–1755.

Hartigan, J.A., Wong, M.A., 1979. Algorithm AS 136: a k-means clustering algorithm. J. R. Stat. Soc. 28, 100–108.

Hilker, T., Wulder, M.A., Coops, N.C., Linke, J., McDermid, G., Masek, J.G., Gao, F., White, J.C., 2009. A new data fusion model for high spatial- and temporal-resolution mapping of forest disturbance based on Landsat and MODIS. Remote Sens. Environ. 113, 1613–1627.

Jacquemoud, S., Verhoef, W., Baret, F., Bacour, C., Zarco-Tejada, P.J., Asner, G.P., François, C., Ustin, S.L., 2009. PROSPECT + SAIL models: a review of use for vegetation characterization. Remote Sens. Environ. 113, 56–66.

Jiang, J., Xiao, Z., Wang, J., Song, J., 2016. Multiscale estimation of leaf area index from satellite observations based on an ensemble multiscale filter. Remote Sens. 8 (3), 229.

Knyazikhin, Y., Martonchik, J.V., Myneni, R.B., Diner, D.J., Running, S.W., 1998. Synergistic algorithm for estimating vegetation canopy leaf area index and fraction of absorbed photosynthetically active radiation from MODIS and MISR data. J. Geophys. Res. 103, 257–275.

Lewis, P., Gomez-Dans, J., Kaminski, T., Settle, J., Quaife, T., Gobron, N., Styles, J., Berger, M., 2012. Data assimilation of sentinel-2 observations: preliminary results from EO-LDAS and Outlook. In: ESA-SP, L.O. (Ed.), First Sentinel-2 Preparatory Symposium. ESRIN, Frascati, Italy.

Li, W., Fang, H., 2015. Estimation of direct, diffuse, and total FPARs from Landsat surface reflectance data and ground-based estimates over six FLUXNET sites. J. Geophys. Res. Biogeo. 120, 96–112.

Li, W., Weiss, M., Waldner, F., Defourny, P., Demarez, V., Morin, D., Hagolle, Olivier, Baret, Frédéric, 2015. A generic algorithm to estimate LAI, FAPAR and FCOVER variables from SPOT4_HRVIR and Landsat sensors: evaluation of the consistency and comparison with ground measurements. Remote Sens. 7, 15494–15516.

Liang, S., Zhao, X., Liu, S., Yuan, W., Cheng, X., Xiao, Z., Zhang, X., Liu, Q., Cheng, J., Tang, H., Qu, Y., Bo, Y., Qu, Y., Ren, H., Yu, K., Townshend, J., 2013. A long-term

Global LAnd Surface Satellite (GLASS) data-set for environmental studies. Int. J. Digital Earth 6 (Sup. 1), 5–33.
Mira, M., Weiss, M., Baret, F., Courault, D., Hagolle, O., Gallego-Elvira, B., Olioso, A., 2015. The MODIS (collection V006) BRDF/albedo product MCD43D: temporal course evaluated over agricultural landscape. Remote Sens. Environ. 170, 216–228.
Semmens, K.A., Anderson, M.C., Kustas, W.P., Gao, F., Alfieri, J.G., McKee, L., Prueger, J.H., Hain, C.R., Cammalleri, C., Yang, Y., Xia, T., Sanchez, L., Mar Alsina, M., Vélez, M., 2016. Monitoring daily evapotranspiration over two California vineyards using Landsat 8 in a multi-sensor data fusion approach. Remote Sens. Environ. 185, 155–170.
Shabanov, N.V., Wang, Y., Buermann, W., Dong, J., Hoffman, S., Smith, G.R., Tian, Y., Knyazikhin, Y., Myneni, R.B., 2003. Effect of foliage spatial heterogeneity in the MODIS LAI and FPAR algorithm over broadleaf forests. Remote Sens. Environ. 85, 410–423.
Verger, A., Baret, F., Camacho, F., 2011a. Optimal modalities for radiative transfer-neural network estimation of canopy biophysical characteristics: evaluation over an agricultural area with CHRIS/PROBA observations. Remote Sens. Environ. 115, 415–426.
Verger, A., Baret, F., Weiss, M., 2011b. A multisensor fusion approach to improve LAI time series. Remote Sens. Environ. 115, 2460–2470.
Verger, A., Baret, F., Weiss, M., Kandasam, S., Vermote, E., 2011c. In: Quantification of LAI interannual anomalies by adjusting climatological patterns. IEEE Transactions on Geoscience and Remote Sensing (AGU Conference).
Weiss, M., Baret, F., 2010. In: fAPAR (fraction of Absorbed Photosynthetically Active Radiation) estimates at various scale. 34th International Symposium on Remote Sensing and Environment (ISRSE). Sydney, Australia.
Weiss, M., Baret, F., Garrigues, S., Lacaze, R., 2007. LAI and fAPAR CYCLOPES global products derived from VEGETATION. Part 2: validation and comparison with MODIS collection 4 products. Remote Sens. Environ. 110, 317–331.
Weng, Q., Fu, P., Gao, F., 2014. Generating daily land surface temperature at Landsat resolution by fusing Landsat and MODIS data. Remote Sens. Environ. 145, 55–67.
Xiao, Z., Liang, S., Sun, R., JindiWang, & Jiang, B., 2015. Estimating the fraction of absorbed photosynthetically active radiation from the MODIS data based GLASS leaf area index product. Remote Sens. Environ. 171, 105–117.
Zhu, X., Chen, J., Gao, F., Chen, X., Masek, J.G., 2010. An enhanced spatial and temporal adaptive reflectance fusion model for complex heterogeneous regions. Remote Sens. Environ. 114, 2610–2623.
Zhu, Z., Woodcock, C.E., Holden, C., Yang, Z., 2015. Generating synthetic Landsat images based on all available Landsat data: predicting Landsat surface reflectance at any given time. Remote Sens. Environ. 162, 67–83.